The EMBO Journal (2011) 30, 652–664 | © 2011 European Molecular Biology Organization | All Rights Reserved 0261-4189/11
www.embojournal.org

THE
EMBO
JOURNAL

Controlled and stochastic retention concentrates dynein at microtubule ends to keep endosomes on track

Martin Schuster[1], Sreedhar Kilaru[1], Peter Ashwin[2], Congping Lin[1,2], Nicholas J Severs[3] and Gero Steinberg[1,*]

[1]School of Biosciences, University of Exeter, Exeter, UK, [2]Mathematics Research Institute, University of Exeter, Exeter, UK and [3]National Heart and Lung Institute, Imperial College London, London, UK

Bidirectional transport of early endosomes (EEs) involves microtubules (MTs) and associated motors. In fungi, the dynein/dynactin motor complex concentrates in a comet-like accumulation at MT plus-ends to receive kinesin-3-delivered EEs for retrograde transport. Here, we analyse the loading of endosomes onto dynein by combining live imaging of photoactivated endosomes and fluorescent dynein with mathematical modelling. Using nuclear pores as an internal calibration standard, we show that the dynein comet consists of ~55 dynein motors. About half of the motors are slowly turned over ($T_{1/2}$: ~98 s) and they are kept at the plus-ends by an active retention mechanism involving an interaction between dynactin and EB1. The other half is more dynamic ($T_{1/2}$: ~10 s) and mathematical modelling suggests that they concentrate at MT ends because of stochastic motor behaviour. When the active retention is impaired by inhibitory peptides, dynein numbers in the comet are reduced to half and ~10% of the EEs fall off the MT plus-ends. Thus, a combination of stochastic accumulation and active retention forms the dynein comet to ensure capturing of arriving organelles by retrograde motors.

The EMBO Journal (2011) **30,** 652–664. doi:10.1038/emboj.2010.360; Published online 28 January 2011
Subject Categories: membranes & transport; cell & tissue architecture
Keywords: dynein; EB1; endosome motility; membrane trafficking; microtubules

Introduction

Bidirectional transport of organelles along microtubules (MTs) is a hallmark of eukaryotic cells, necessary for cellular organization and survival (Welte, 2004). In mammalian neurons, MT-dependent retrograde transport of early endosomes (EEs) mediates communication between the synapses and the cell nucleus, thereby preventing the cell from undergoing controlled cell death (Miaczynska *et al*, 2004; Howe and Mobley, 2005; Chevalier-Larsen and Holzbaur, 2006). Retrograde motility of EEs is mediated by dynein and the associated dynactin complex (Schroer, 2004; Vallee *et al*, 2004). It was shown that dynactin interacts with the plus-end binding protein EB1 (Ligon *et al*, 2003; Honnappa *et al*, 2006; Akhmanova and Steinmetz, 2008) thereby establishing a loading site that captures EEs (Valetti *et al*, 1999), melanophores (Lomakin *et al*, 2009) and Golgi membranes (Vaughan *et al*, 2002; Vaughan, 2005). Phosphorylation of mammalian dynactin compound p150^{glued} releases the complex from MT plus-ends (Vaughan *et al*, 2002), indicating that regulatory mechanisms control the concentration and the dynamics of the transport machinery at MT ends. This is in line with numerous reports, showing active regulation of motor proteins and membrane transport (Kumar *et al*, 2000; Andersson *et al*, 2003; Deacon *et al*, 2005; Ally *et al*, 2008). However, an increasing number of reports have detailed the stochastic behaviour of motors (Klumpp and Lipowsky, 2005; Müller *et al*, 2008; Gazzola *et al*, 2009), raising the possibility that stochastic transport processes and active regulation cooperate to control cargo transport (Welte and Gross, 2008).

The genetically tractable filamentous fungus *Ustilago maydis* shares many proteins with humans that are not encoded in the model fungus *Saccharomyces cerevisiae* (Münsterkötter and Steinberg, 2007). It is therefore a good model system for the role of MTs in long-range transport (Steinberg and Perez-Martin, 2008). Similar to human cells (Hoepfner *et al*, 2005) and the ameba *Dictyostelium discoideum* (Soppina *et al*, 2009), kinesin-3 transports EEs to MT plus-ends (anterograde; Wedlich-Söldner *et al*, 2002a; Lenz *et al*, 2006), which are concentrated at the hyphal tip (Schuchardt *et al*, 2005). There, the EEs support recycling processes required for polarized growth and mating of the fungus (Wedlich-Söldner *et al*, 2000; Fuchs *et al*, 2006). It was suggested that retrograde transport of the EEs might mediate long-range communication to the nucleus (Steinberg, 2007). The motility back to the cell centre is initiated by binding of the organelles to dynein, which concentrates in a comet-like accumulation at apical MT plus-ends (Xiang, 2003; Lenz *et al*, 2006; Abenza *et al*, 2009; Zhang *et al*, 2010). How EEs are loaded onto dynein is not clear, but effective interaction of the motor and the cargo is required to ensure that the arriving organelles do not fall off the MT end. In this study, we provide evidence that dynein captures EEs in a stochastic way. In order to increase the probability of kinesin-3-delivered EEs, our study suggests that the cell raises the number of dynein motors by stochastic retention and a controlled interaction between EB1 and dynactin. This mechanism ensures efficient loading of EEs onto dynein and prevents the organelles from falling off the track at MT ends.

---

*Corresponding author. School of Biosciences, University of Exeter, Stocker Road, Exeter EX4 4QD, UK. Tel.: +44 139 226 3476; Fax: +44 139 226 3434; E-mail: g.steinberg@exeter.ac.uk

Received: 21 May 2010; accepted: 21 December 2010; published online: 28 January 2011

Results

Endosomes are rapidly loaded onto apical dynein

Hyphal cells of the filamentous fungus *U. maydis* are elongated and expand at their tip (Figure 1A, asterisk), where the MT plus-ends are concentrated (Schuchardt *et al*, 2005). To visualize the endogenous level of dynein, we integrated three tandem copies of green-fluorescent protein (GFP) into the native locus of the dynein heavy chain gene *dyn2* (for genotype of all strains see Table I). Cells expressing the fusion protein (GFP_3–Dyn2) were growing normally, whereas dynein mutants are morphologically defective (Supplementary Figure S1), suggesting that the fusion protein was biologically active. We next improved our microscopic setup by using solid-state lasers instead of conventional illumination in wide-field epifluorescence microscopy. In doing so, we were able to visualize strong signals of dynein concentrated at apical MT ends, labelled by the EB1-homolouge Peb1 (Straube *et al*, 2003) fused to mRFP (Figure 1B, dynein intensity given in false colours; Supplementary Figure S2). In addition to the apical concentration of dynein, we observed fast moving dynein signals along the length of the hypha (Supplementary Movie 1).

It was reported that kinesin-3 takes EEs to MT plus-ends at the hyphal tip where they become loaded onto the apical dynein for retrograde motility (Lenz *et al*, 2006). To investigate this, we visualize individual EEs by fusing photoactivatable GFP (paGFP; Patterson and Lippincott-Schwartz, 2002) to the small GTPase Rab5a that was shown to reside on EEs (Fuchs *et al*, 2006). When activated by 405 nm laser light, EEs became visible and in most cases moved to MT plus-ends before turning for retrograde motility (Supplementary Movie 2). Motility of the organelles was readily visualized in kymographs, which are graphical representation of spatial position over time (Figure 1C). We found that 0.7 ± 0.2 (sample size, $n = 151$) EEs reached the hyphal tip per second, where 88% of the organelles rapidly turned around within <1 s (Figure 1D, 'Turning'; Figure 1E). The loading of EEs onto dynein was very efficient, with only 1.74% of all EEs ($n = 800$) falling off the MT (Figure 1D, 'Detaching'), as indicated by random Brownian motion at the cell end (Supplementary Movie 3). It was suggested that arriving endosomes activate dynein at the MT plus-end for retrograde motility (Lenz *et al*, 2006). To test this, we expressed a mutant kinesin-3 protein that blocks EE motility by anchoring EEs to MTs ($Kin3^{rigor}$; Wedlich-Söldner *et al*, 2002a). When expressed in hyphae, EEs remained stationary and did not arrive at the apical dynein comet (Figure 2A). However, in such mutants dynein was still able to leave the MT end at normal velocity and rates (Figure 2B and C).

A large number of dyneins form the comet at MT plus-ends

The apical dynein comets showed very strong fluorescence and co-localized with the EB1-homolouge Peb1 (see above),

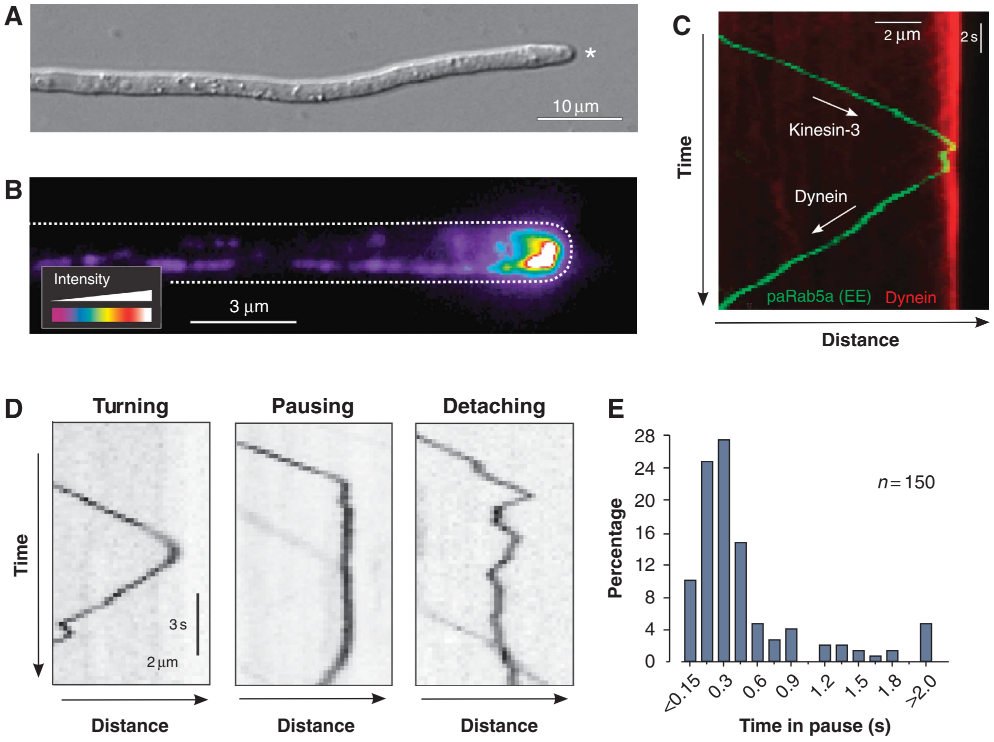

Figure 1 Loading of photoactivated EEs onto dynein at the apical MT plus-ends. (**A**) Hyphal cell of *U. maydis*. The cell elongated by polar extension at the tip (asterisk). Note that MTs in the apical region show a unipolar orientation with plus-ends directed to the cell tip (Lenz *et al*, 2006). The bar represents micrometers. (**B**) Pseudo-coloured image of dynein in the apex of a hyphal cell. The endogenous dynein heavy chain was tagged with 3 × GFP (strain $AB33G_3Dyn2$, see Table I for genotypes of all strains). Most dynein accumulates at the growth region of the cell. Cell edge is indicated with a dotted line. The bar represents micrometers. (**C**) Kymograph showing anterograde delivery of an EE to the dynein comet. The organelle is labelled by paGFP-Rab5a (green), the comet is visualized by a fusion protein of the dynein heavy chain and triple tag of monomeric Cherry (red). The motors delivering the EEs is kinesin-3 (Lenz *et al*, 2006). The bars represent micrometers and seconds. (**D**) Kymographs showing the behaviour of paGFP-Rab5a-carrying EEs at an apical MT end. Detaching is characterized by irregular Brownian motion. Note that pausing and detaching are rare events. The bars represent micrometers and seconds. Inverted contrast is shown. (**E**) Bar chart showing pausing time of EEs at apical MT plus-ends. Most EEs turn within 1 s.

Table I Strains and plasmids used in this study

AB33G$_3$Dyn2	*a2* P*nar-bW2* P*nar-bE1*, P*dyn2-3xegfp-dyn2, ble*^{R}*, hyg*^{R}	Lenz *et al* (2006)
AB33Dyn2Ch$_3$_paGRab5a	*a2* P*narbW2* P*narbE1,* P*dyn2-dyn2-3xmcherry, ble*^{R}, *nat*^{R}/popaGRab5a	This study
AB33GRab5a	*a2* P*narbW2* P*narbE1, ble*^{R}/poGRab5a	This study
FB1Dyn2^{ts}	*a1b1 Pdyn2-dyn2*^{ts}*, nat*^{R}	Wedlich-Söldner *et al* (2002b)
FB2N107G_ER	*a2b2* P*nup107-nup107-egfp*, *ble*^{R}/pERRFP	Theisen *et al* (2008)
FB2N107R_N214G	*a2b2* P*nup107-nup107-mrfp*, P*nup214-nup214-egfp, hyg*^{R}, *ble*^{R}	Theisen *et al* (2008)
FB2N214G$_3$	*a2b2* P*nup214-nup214-3egfp, hyg*^{R}	This study
FB2N107G_ N214G$_2$	*a2b2* P*nup107-nup107-egfp*, P*nup214-nup214-2egfp, ble*^{R} *hyg*^{R}	This study
FB2N107G_ N214G$_3$	*a2b2* P*nup107-nup107-egfp*, P*nup214-nup214-3egfp, ble*^{R} *hyg*^{R}	This study
FB2N107G_ N214G$_3$_N2G	*a2b2* P*nup107-nup107-egfp*, P*nup214-nup214-3egfp,* P*nup2-nup2-egfp, ble*^{R} *hyg*^{R}, *nat*^{R}	This study
AB33GRab5 _rKin3^{G105E}	*a2* P*narbW2* P*narbE1*/*ble*^{R}/poGRab5a/pcrgKin3^{G105E}	This study
AB33G$_3$Dyn2 _rKin3^{G105E}	*a2* P*narbW2* P*narbE1* P*dyn2-3xegfp-dyn2 ble*^{R}, *hyg*^{R}/pcrgKin3^{G105E}	This study
AB33pa$_m$G$_3$Dyn2	*a2* P*nar-bW2* P*nar-bE1*, P*dyn2-3xpamgfp-dyn2, ble*^{R}*, hyg*^{R}	This study
AB33G$_3$Dyn2 _Peb1R	*a2* P*nar-bW2* P*nar-bE1*, P*dyn2-3xegfp-dyn2,* P*peb1-peb1-mrfp, ble*^{R}*, hyg*^{R}, *nat*^{R}	This study
AB33G$_3$Dyn2 _cEB1	*a2* P*narbW2* P*narbE1* P*dyn2-3xegfp-dyn2 ble*^{R}, *hyg*^{R}/pcrgPeb1$^{211-268}$	This study
AB33G$_3$Dyn2 _nDya1	*a2* P*narbW2* P*narbE1* P*dyn2-3xegfp-dyn2 ble*^{R}, *hyg*^{R}/pcrgDya1$^{32-62}$	This study
AB33G$_3$Dyn2 _nDya1*	*a2* P*narbW2* P*narbE1* P*dyn2-3xegfp-dyn2 ble*^{R}, *hyg*^{R}/pcrgDya1$^{32-62,\ Q35E}$	This study
AB33pa$_m$G$_3$Dyn2 _cEB1	*a2* P*narbW2* P*narbE1* P*dyn2-3xpamgfp-dyn2 ble*^{R}, *hyg*^{R}/pcrgPeb1$^{211-268}$	This study
AB33pa$_m$GRab5a_cEB1	*a2* P*narbW2* P*narbE1*/popaGRab5a/pcrgPeb1$^{211-268}$	This study
popaGRab5a	P*otef-pagfp-rab5a, cbx*^{R}	This study
poGRab5a	P*otef-egfp-rab5a, nat*^{R}	This study
pERRFP	P*otef-cal*^{s}*-mrfp*-HDEL*, cbx*^{R}	Theisen *et al* (2008)
pcrgKin3^{G105E}	P*crg-kin3*^{G105E}*, cbx*^{R}	Wedlich-Söldner *et al* (2002a)
pcrgPeb1$^{211-268}$	P*crg-peb1*$^{211-268}$*, cbx*^{R}	This study
pcrgDya1$^{32-62}$	P*crg-dya1*$^{32-62}$*, cbx*^{R}	This study
pcrgDya1$^{32-62\ Q35E}$	P*crg-dya1*$^{32-62,\ Q35E}$*, cbx*^{R}	This study

a, b, mating type loci; P, promoter; -, fusion; *hyg*^{R}, hygromycin resistance; *ble*^{R}, phleomycin resistance; *nat*^{R}, nourseothricin resistance; *cbx*^{R}, carboxin resistance; ^{ts}, temperature-sensitive allele; /, ectopically integrated; *crg*, conditional arabinose-induced promoter; *otef*, constitutive promoter; *nar*, conditional nitrate reductase promoter; *E1*, *W2*, genes of the *b* mating type locus; *nup2*, *nup107, nup214* nucleoporins; HDEL, ER retention signal; *egfp*, enhanced green-fluorescent protein; *pamgfp:* photoactivatable monomeric green-fluorescent protein*; mrfp*, monomeric red-fluorescent protein; *mcherry*, monomeric cherry; *peb1*$^{211-268}$, fragment of EB1-like plus-end binding protein; *dya1*$^{32-62}$, fragment of the dynactin subunit p150Glued; *dya1*$^{32-62Q35E}$, point mutated fragment of the dynactin subunit p150Glued; *dyn2*: C-terminal half of the dynein heavy chain; *peb1*, EB1-like plus-end binding protein; *rab5a*, small endosomal Rab5-like GTPase; *kin3*^{G105E}, rigor allele of kinesin3.

indicating that numerous motors accumulate at MT plus-ends. To determine the number of motors within the comets, we established an internal calibration standard to which our measurements could be related. Such a correlative approach was successfully used to obtain accurate numbers of GFP-labelled proteins in *S. cerevisiae* (Joglekar *et al*, 2008). We chose the nuclear pore complex because it is a highly ordered and conserved structure that contains 16 copies of the nucleoporin Nup107/84 and 8 copies of Nup214/159 (Rabut *et al*, 2004).

When GFP was fused to the endogenous *nup107* gene, we found Nup107-GFP in spots within the nuclear envelope (Figure 3A, left panel) that showed a homogeneous fluorescence intensity (Figure 3A, right panel, intensity given in false colours) and that represent nuclear pores as confirmed by freeze-fracture electron microscopy (Figure 3A, middle panel). We next confirmed that each pore contains 16 copies of Nup107-GFP by comparing it to native levels of Nup214-GFP, a nucleoporin that is generally found in 8 copies (Rabut *et al*, 2004). We fused GFP to the native copy of *nup214* and determined the number of GFPs by stepwise photobleaching, a method used to analyse protein numbers in the living cell (Cai *et al*, 2007; Ulbrich and Isacoff, 2007; Hendricks *et al*, 2010). We found that Nup214-GFP bleached in at most eight steps (Figure 3B) in agreement with the observation that GFP-107 signals were twice as strong as GFP-214 (Figure 3C; N107G, N214G), indicating that 16 copies of Nup107-GFP reside in a single nuclear pore.

The fluorescent intensity of GFP in the dynein comet was much stronger than that of a Nup107-GFP containing nuclear pore, suggesting that numerous dyneins make up the comet. We therefore investigated whether an increased number of GFP tags result in a linear increase in fluorescence. To this end, we generated strains that simultaneously expressed various combinations of Nup107-GFP, Nup214 fused to double or triple GFP and GFP fused to Nup2, another nucleoporin identified in *U. maydis* (Theisen *et al*, 2008; see Supplementary data for more details). We found that the intensity of fluorescence in individual pores linear increased with the number of GFP tags (Figure 3C). This allowed us to estimate the number of GFP tags (and thereby the number of dynein motors) in the comet by determining the mean value of the Nup107-GFP intensity in single pores (=16 GFP; distribution for single GFP shown in Figure 3D). The dynein heavy chain dimerizes and when tagged with triple GFP, a single motor is expected to carry 6 GFP tags. As no indication of proteolytic degradation of GFP$_3$–Dyn3 was found in cell extracts (Supplementary Figure S3), we used the average intensity for a single GFP derived from our internal calibration standard to estimate the dynein number in the comets. This analysis revealed that ∼55 dynein motors are concentrated in a dynein comet (Figure 3E).

Two different populations of dynein are found in the apical comet

Our results suggested that a large number of dynein motors accumulate at the apical MT ends. To further characterize this dynein comet, we fused a triple tag of photoactivatable GFP to the endogenous copy of the dynein heavy chain gene *dyn2*. Again, this modification did not affect the cell, indicating that

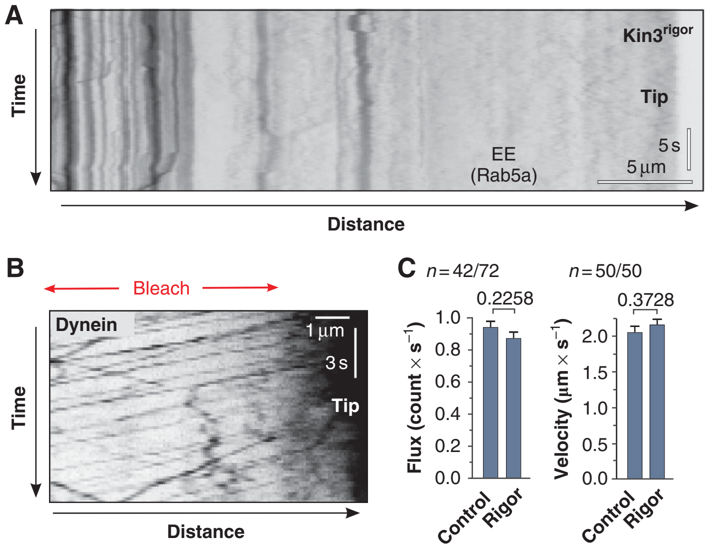

Figure 2 EE-independent retrograde motility of dynein. (**A**) Kymograph showing frozen EE motility in a hypha that overexpresses Kin3^{rigor} (strain AB33GRab5_rKin3^{G105E}). Vertical lines indicate stationary EEs and no cargo reaches the hyphal tip (Tip). The bars represent micrometers and seconds. Inverted contrast is shown. (**B**) Kymograph of a hyphal tip in cells expressing Kin3^{rigor} (strain AB33G$_3$Dyn2_rKin3^{G105E}). Despite the block in cargo motility dynein undergoes retrograde motility. This is best seen after photobleaching the subapical region of the hypha (Bleach). The bars represent micrometers and seconds. Inverted contrast is shown. (**C**) Bar charts showing a quantitative analysis of retrograde motility of dynein signals in control cells and cells that express Kin3^{rigor}. Both frequency and velocity of retrograde dynein motility are unaffected. *P*-values derived from two-tailed Student's *t*-tests are given above bars. Values are mean ± standard error of the mean; sample size *n* is given.

the fusion protein is biologically functional (Supplementary Figure S1). When activated at the apical MT plus-ends, paGFP$_3$–Dyn2 continuously left the MT end and the signal gradually decreased (Figure 4A; Supplementary Movie 4; note that in this movie photobleaching also gives this effect, and this was taken into account in the subsequent quantitative analysis). Non-linear regression of the decay curve favoured a two-phase decay over one-phase decay (Figure 4B; F-test gives $P<0.0001$: $F=20.34$; $DFn=2$, $DFd=171$). This suggested the existence of two populations of dynein, with about half (31–65% for 95% confidence interval) of the dynein signals rapidly leaving ($T_{1/2}$: 10.2 s; 3.7–16.7 s for 95% confidence interval) and the other half (35–69% for 95% confidence interval) staying significantly longer ($T_{1/2}$: 98.0 s; 61.4–134.6 s for 95% confidence interval). To obtain independent evidence for this result we performed fluorescent recovery after photobleaching (FRAP) experiments. When GFP$_3$–Dyn2 in the apical dynein comet was photobleached, delivery of dynein rapidly recovered the signal, again following a two-phase exponential curve (Figure 4C; F-test gives $P<0.0001$: $F=15.36$; $DFn=2$, $DFd=150$) with half-life times very similar to the previous experiment with $T_{1/2}$: 10.23 s (0.09061–20.37 s for 95% confidence interval) and $T_{1/2}$: 89.97 s (57.65–122.3 s for 95% confidence interval).

An interaction between dynactin and EB1 retains half of the dynein in the comet

We next consider the mechanism by which dynein is held at MT plus-ends. In mammalian cells, the dynactin complex, which binds dynein, is anchored to MT plus-ends by an interaction with the plus-end binding protein EB1 (Ligon *et al*, 2003), and the interaction site is well characterized in humans (Honnappa *et al*, 2006). In *U. maydis*, the EB1-homologue Peb1 also co-localizes with dynein (see above), and the p150^{glued} dynactin compound Dya1 also concentrate at MT plus-ends (Lenz *et al*, 2006). Furthermore, the primary amino-acid sequence of the interaction site is highly conserved (Figure 4D). This suggested that dynein might be anchored to MT plus-ends by an interaction of Peb1 and Dya1. To test this, we generated two peptides, Peb1c and Dya1n, which covered the predicted interacting amino acids in both proteins (Figure 4D). Indeed, high expression of both peptides led to a significant decrease of the amount of dynein at MT plus-ends (Figure 4E and F). This reduction was not found when a Dya1 peptide was expressed that contained a point mutation known to inhibit the binding to EB1 (Figure 4D and F; Dya1n*; Honnappa *et al*, 2006). This suggests that the inhibitory effect of Peb1c and Dya1n is due to a specific blockage of the interaction of the EB1 homologue and dynactin. Surprisingly, the inhibitory peptides were only able to remove ~60% of the dynein from MT ends (Figure 4F). This result was in agreement with the finding of two populations of dynein that differ in their turnover at MT ends. These data suggested that anchorage of dynein impairs its release and, consequently, the remaining ~40% of dynein represent the more dynamic population. To test this, we expressed the inhibitory peptide Peb1c in cells containing paGFP$_3$–Dyn2 and analysed the decay of the remaining comet. We found that under these conditions, the photoactivatable dynein is released in one-phase decay reaching a plateau of 4.5% (favoured over a two-phase decay; F-test at $P=0.9276$; $F=0.07515$; $DFn=2$, $DFd=141$), with a rapid half-life time of 20.88 s (18.15–23.65 s for 95% confidence interval; Figure 4G), suggesting that it indeed represents the dynamic population. In summary, these results suggest that a dynein comet builds up by active retention via an interaction of dynactin and EB1. However, a second, EB1/dynactin-

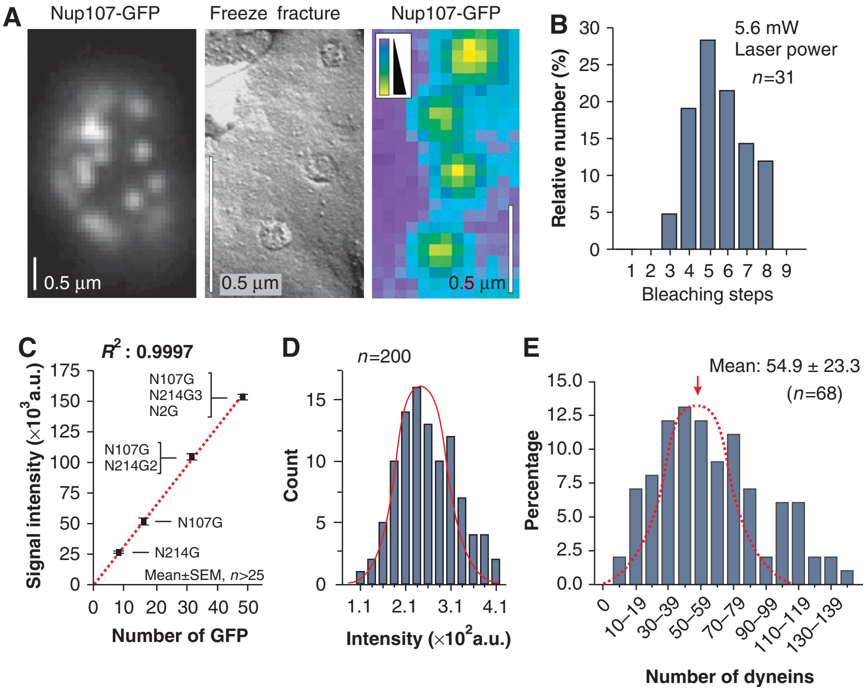

Figure 3 Nuclear pores as internal calibration standard for quantitative fluorescence intensity measurements. (**A**) The endogenous copy of the nucleoporin Nup107 was fused to GFP and the fusion protein labels nuclear pores (left panel, Nup107-GFP). Freeze-fracture electron microscopy confirms that these signals represent single pores (middle panel, freeze fracture), which often show uniform signal intensity (right panel, Nup107-GFP, false-coloured image). The bars represent 0.5 μm. (**B**) Bleaching-step analysis of Nup214-GFP in nuclear pores. Note that the endogenous *nup214* gene was fused to GFP. Bleaching steps from 3 to maximal 8 was found. This demonstrates that 8 copies of Nup214 reside in single nuclear pores. (**C**) Fluorescence intensity of nuclear pores containing Nup214-GFP (N214G), Nup107-GFP (N107G), Nup107-GFP + Nup214-GFP$_2$ (N107G/N214G2) and Nup107-GFP + Nup214-GFP$_3$ + Nup2-GFP (N107G/N214G3/N2G). The increase in fluorescent intensity is linear. The regression coefficient R^2 is given. Values are mean ± standard error of the mean, sample size n is given. Note that all GFP tags were fused to the endogenous genes. (**D**) Bar chart showing the signal intensity distribution of Nup107-GFP in nuclear pores. The measurements fit a Gaussian distribution (red line). Note that absolute values differ from those in C due to different experimental conditions used in these particular experiments (e.g. laser power and exposure time). (**E**) Bar chart showing the estimated number of dynein motors in comets at MT plus-ends. Note that most of the population follows a Gaussian distribution (red dotted line). Larger numbers might reflect two adjacent comets and were therefore excluded from the calculation of the mean.

independent mechanism helps to increase the number of dyneins at apical MT ends.

Transport properties of antergrade and retrograde dynein motility

It was previously shown that *in vitro* molecular motors can accumulate at MT ends thereby forming ‘comet-like’ structures (Okada and Hirokawa, 1999). This phenomenon does not involve any active regulation but can be understood as a consequence of queuing of motors, and we considered it possible that dynein concentrates at the MT plus-end in a similar stochastic way. We aimed to analyse this possibility by developing a mathematical model to describe the formation of the dynein comet. To generate a robust model, we set out to raise quantitative data about dynein motility in our cell system. We analysed GFP$_3$–Dyn2 movements in greater detail near the hyphal tip, where MTs have a unipolar orientation (Lenz *et al*, 2006). After photobleaching this region, anterograde and retrograde motility of GFP$_3$–Dyn2 signals became easily visible (Figure 5A). Individual signals moved in both directions at similar velocities ($V_{\mathrm{anterograde}} = 1.66 \pm 0.37$ μm/s, $n = 202$; $V_{\mathrm{retrograde}} = 1.76 \pm 0.55$ μm/s, $n = 209$), and signals sometimes turned direction (Figure 5A; arrowhead, lower panel), with 2.39% of the motors ($n = 300$) turning from anterograde to retrograde motility and 1.60% ($n = 300$) turning from retrograde to anterograde motility per 1 μm travelled (see Supplementary data). To analyse the frequencies of transport towards and away from the MT plus-ends, we set out to determine the number of dynein motors per moving signal. Motor numbers were previously determined by stepwise photobleaching (Cai *et al*, 2007; Hammond *et al*, 2009; Hendricks *et al*, 2010). To apply this method to moving dynein signals, we reduced interference by photobleaching large parts of the hyphal cell. In addition, we treated the cells with cyanide 3-chlorophenyl-hydrazone (CCCP), a drug that reversibly inhibits cell respiration resulting in reduced ATP levels. This treatment gradually immobilized the dynein and allowed accurate bleaching-step analysis. In a typical experiment, GFP$_3$–Dyn2 was photobleached in the subapical regions. From unbleached parts at the cell tip dynein moved retrograde into the darkened area before it got immobilized by the depletion of ATP (Figure 5B, yellow arrows). Thus, the signals could be recognized as retrograde dynein and were analysed for stepwise bleaching. We found that the majority of the retrograde, as well as the anterograde GFP$_3$–Dyn2 signals bleached in up to six steps (Figure 5C and D), suggesting that they represent a single dynein motor. This was confirmed by comparison of their fluorescence intensity with our nuclear pore calibration standard, again showing that most signals are single dynein motors (Figure 5E). Statistical analysis using the bleaching-step curves revealed that the proportion of single-to-double

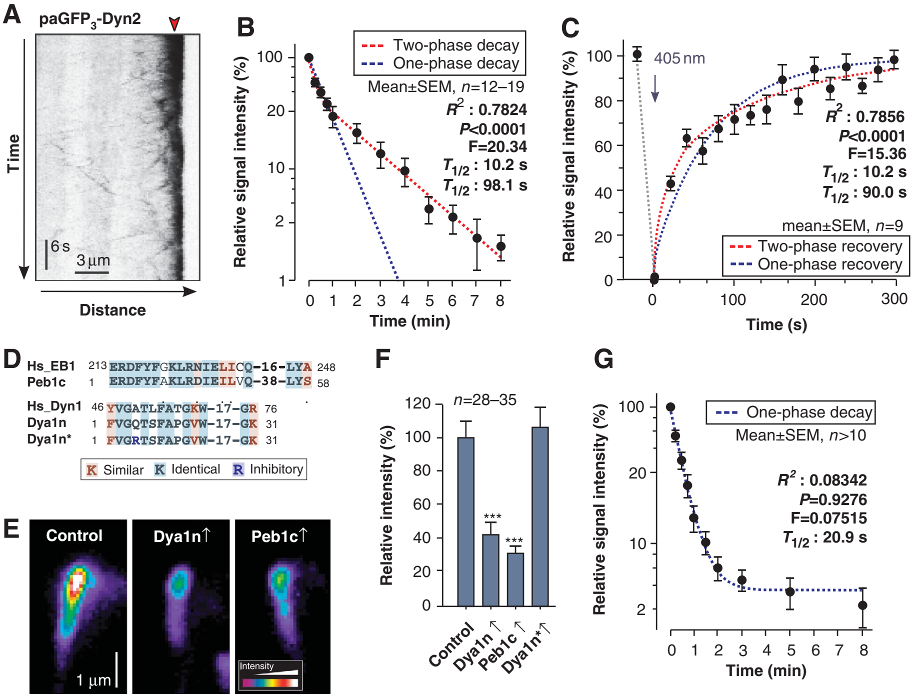

Figure 4 Experimental evidence for two populations of dynein at MT plus-ends. (**A**) Kymograph showing the decay of photoactivatable dynein at the hyphal tip (strain AB33pa$_m$G$_3$Dyn2). Note that the endogenous dynein heavy chain was tagged with a triple tandem repeat of photoactivatable GFP. Point of activation by a 405-nm laser is indicated with red arrowhead. Note that under continuous observation, photobleaching also reduces the apical dynein signals. (**B**) Decay of photoactivatable dynein after activation at MT plus-ends. The decay follows a two-phase decay curve (red dotted line) that strongly favoured over one-phase decay (blue dotted line; F-test, $P<0.0001$). R^2 for two-phase exponential decay, F-test results and predicted half-life times are given. The *Y*-axis is given in log-scale. Values are mean ± standard error of the mean; sample size *n* is given. The decrease of fluorescent intensity that was due to release from the MT plus-ends was measured in intervals to account for bleaching effects. (**C**) Fluorescence recovery of GFP$_3$-dynein heavy chain at MT plus-ends after photobleaching. The recovery follows a two-phase curve (red dotted line) that is strongly favoured over one-phase recovery (blue dotted line; F-test, $P<0.0001$). R^2 for two-phase exponential recovery, F-test results and predicted half-life times are given. Values are mean ± standard error of the mean; sample size *n* is given. The 405-nm bleaching laser pulse is indicated with an arrow. The increase of fluorescent intensity was measured in intervals to account for bleaching effects. (**D**) Sequence comparison of EB1 and the dynactin compound p150$^{\text{glued}}$ from human (Hs_EB1, Hs_Dyn1) with the inhibitory peptides Peb1c and Dya1n, which reflect the sequence of the EB1- and p150$^{\text{glued}}$ counterparts in *U. maydis* (Peb1c, Dya1n). The peptide Dya1n* contains a point mutation (blue) that was shown to inhibit binding of dynactin to EB1 (Honnappa *et al*, 2006). (**E**) Pseudo-coloured images of dynein signals at MT plus-ends of control cells (control) and cells that express the inhibitory peptides Peb1c (strain AB33G$_3$Dyn2_rEB1$^{211-268}$) and Dya1n (strain AB33G$_3$Dyn2_rDya1$^{32-62}$). Expression of peptides covering the interface between EB1 (Peb1c) and p150$^{\text{glued}}$ (Dya1n) results in a significant reduction of the amount of dynein at MT ends. (**F**) Bar chart showing the effect of high expression of the peptides Dya1n, Peb1c and the mutant peptide Dya1n* on the amount of dynein at apical MT plus-ends. Triple asterisks indicate significant difference to control at $P<0.0001$. All bars are given as mean ± standard error of the mean. Note that the control peptide Dya1n* contains an inhibitory point mutation that should prevent its binding to EB1 and therefore was expected to have no effect of dynein numbers at the MT plus-ends. (**G**) Decay of photoactivatable dynein after activation at MT plus-ends in cells that express Peb1c, which interferes with dynein anchorage. The decay follows a one-phase decay curve to a plateau of 4.5% (blue dotted line) that is strongly favoured over a two-phase decay. R^2 coefficient, F-test results and predicted half-life times are given for the one-phase exponential decay to a plateau. The *Y*-axis is given in log-scale. Values are mean ± standard error of the mean; a sample size *n* is given. The decrease of fluorescent intensity that was due to release from the MT plus-ends was measured in intervals to account for bleaching effects.

dyneins was found to be 3.998:1 ($n=77$) for retrograde and 8.492:1 ($n=56$) for anterograde moving GFP$_3$–Dyn2 signals. These ratios were used, along with the frequency of signal movement to estimate that the flux at which dynein enters (Flux$_{\text{anterograde}}$) and leaves (Flux$_{\text{retrograde}}$) the apical region. We estimated a rate 1.06 dynein/second for both directions, which further was included in the mathematical modelling (see below; see Materials and methods for further details).

Mathematical modelling suggests that dynein accumulates stochastically

Having determined the motility parameters and motors numbers, we constructed a stochastic model for the bidirectional motility behaviour of dynein based on asymmetric simple exclusion process (ASEP) models of biological transport processes (Chowdhury *et al*, 2005). We simulated dynein motility using a published two-lane model that assumes that motors move on two lanes (Supplementary Figure S4; Ashwin *et al*, 2010). Using our experimental rates and velocities, this model produced kymographs that show remarkable similarities to our experimental results (Figure 6A) and predicted an accumulation of dynein at the MT end (Supplementary Movie 5). However, the simple two-lane model did not take into account that MTs consist of 13 protofilaments (Tilney *et al*, 1973), or that dynein changes lanes frequently (Wang *et al*, 1995), whereas kinesin-1 does not change lanes (Ray *et al*, 1993). Furthermore, we recognized that the cytoplasmic background of GFP$_3$–Dyn2 in the apex is higher than in the subapical cytoplasm

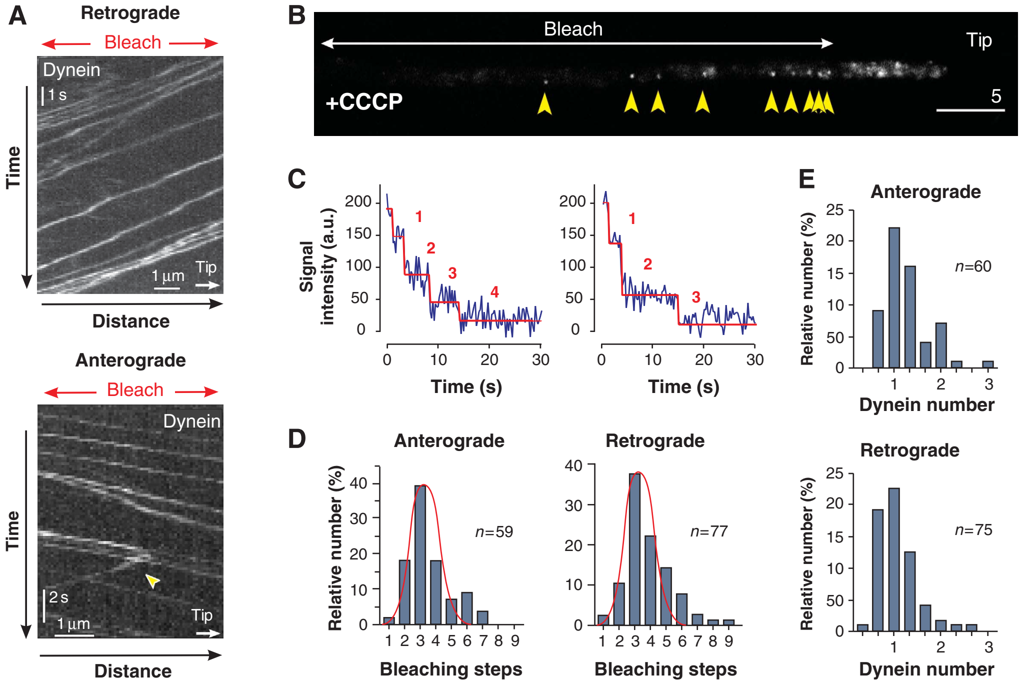

Figure 5 Motility behaviour and quantitative analysis of motor numbers in moving dynein signals. (**A**) Kymograph showing anterograde and retrograde motility of GFP$_3$–Dyn2. The analysis was restricted to the apical 10 µm, where MTs are unipolar oriented (Lenz *et al*, 2006). To avoid interference, the apical region was photobleached (Bleach) and the velocity, frequency and turning (arrowhead) of signals that moved into the darkened part of the cell was analysed. The bars represent micrometers and seconds. (**B**) GFP$_3$–Dyn2 signals in a photobleached cell that was placed on 100 µM CCCP for 15 min. Motors entered the darkened region from the unbleached hyphal tip at the right (Tip). CCCP inhibits the respiration chain and quickly leads to a drop in ATP levels, which in turn immobilized GFP$_3$–Dyn2 within the bleached part of the hypha (yellow arrowheads). The number of GFP tags in these signals was investigated by quantitative bleaching-step analysis. The bars represent micrometers and seconds. (**C**) Bleaching curves showing bleaching steps of GFP$_3$–Dyn2 signals after immobilization with CCCP. Step analysis was done with the algorithm STEPFINDER (Kerssemakers *et al*, 2006). Predicted bleaching steps are indicated with red numbers. (**D**) Bar chart showing the distribution of bleaching steps for anterograde and retrograde signals. In both cases, the majority fits to a normal distribution with a maximum at 3–4 bleaching steps (red curve in bar charts), indicating that they are single dynein motors, containing 6 GFP in a dimer of GFP$_3$–Dyn2. (**E**) Bar charts showing an estimation of dynein numbers in fluorescent signals derived from comparison with Nup107-GFP as internal calibration standard. Again, most anterograde and retrograde GFP$_3$–Dyn2 signals are predicted to represent single dynein motors.

(Supplementary Figure S5), suggesting some dynein detachment at MT plus-ends, again a possibility that is excluded in the two-lane model (Ashwin *et al*, 2010). We therefore extended the two-lane model to a more realistic 13-lane scenario that took these observations and conditions into account. It assumes that motors undertake 8 nm steps (Schnitzer and Block, 1997; Reck-Peterson *et al*, 2006) at certain probabilities (Figure 6B) and that the behaviour of motors is homogeneous along the MT (e.g. no change of turning rates at the MT tip). Finally, we included a 2% loss of arriving dynein, which reflects the escape rate for EEs at plus-ends (see above; for further details see Supplementary data). In this model, motor collisions are resolved by dynein changing lanes (Supplementary Figure S6). We assume that the probability for this side stepping (P_6; Figure 6B) is the same as the measured probability of dynein changing lanes without running into an obstacle (Wang *et al*, 1995; P_5; Figure 6B). Under these conditions, the 13-lane model predicted the accumulation of 25.4 ± 0.2 (mean ± s.e.m., $n = 400$) dyneins at MT plus-ends ($P_6 = P_5$; Figure 6D; Supplementary Movie 6). We realized that P_6 is an estimate that is not supported by experimental data. We therefore investigated the degree to which alterations in P_6 influence the comet size. First, we considered the possibility that motor collision increases P_6, allowing dynein moving forward without any delay ($P_6 = \frac{1}{2}P_1$). Second, we considered the possibility that collisions decrease P_6 but blockages clear faster than we can resolve in the experiments ($P_6 = P_7$). Simulations based on these P_6 values showed very little difference in the comet size (Figure 6C). Thus, the 13-lane model predicts that homogeneous stochastic transport processes could account for the dynamic accumulation of dynein in the comet. However, breaking the homogeneity, for example by setting a different turning probability P_2(tip) within the first 500 nm of the MT, affects the dynein number at plus-ends (Figure 6D). This reinforces the observation that local conditions at the plus-end, such as the reported interaction with EB1, can have a strong influence on the comet size.

The high number in the dynein comet is required to keep EEs on the track

In contrast to our previous model of dynein loading, EEs seem not to activate dynein, which suggests that loading of the organelles onto dynein is a stochastic process. Such a concept would imply that a higher amount of dynein at the tip should result in an increase in EE turning from anterograde to retrograde motility. Indeed, the results described so far indicated that the cell actively increases the number of dynein motors at MT plus-ends. Assuming a stochastic loading process, we considered it possible that the high dynein

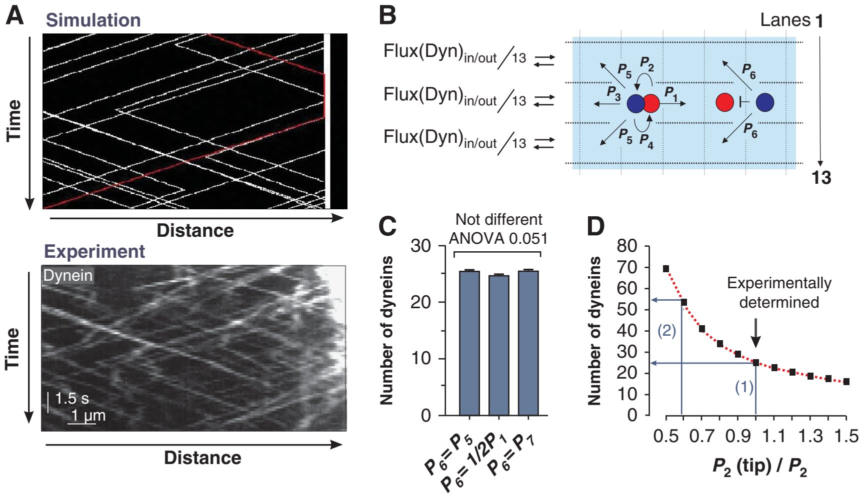

Figure 6 A stochastic model for dynein dynamics at MT plus-ends. (**A**) Comparison of kymographs of dynein motility derived from the two-lane model (Ashwin *et al*, 2010) showing computer simulations (Simulation) and experimental observation (Experiment). The bars represent micrometers and seconds. (**B**) The stochastic 13-lane model for dynein motility near a MT plus-end. At each time step, each motor has the illustrated probabilities (P_1–P_6) of moving in various directions. The model includes collisions between motors and detachment at the MT plus-end. For further conditions see main text and Supplementary data. (**C**) Model prediction of the dynein comet size at the MT plus-end for three different values of P_6. Variations in the probability of dynein changing lanes when meeting kinesin-1 on the same lane (P_6) are (1) meeting the obstacle has no influence on dynein changing lanes ($P_6=P_5$); (2) dynein changes lane with higher probability ($P_6=\frac{1}{2}P_2$); and (3) the probability P_6 is reduced, but blockage of motility is still too fast to be recognized in kymographs ($P_6=P_7$). All simulations predict ∼25 dynein motors in the comet. All bars are given as mean ± standard error of the mean; the sample size is 400 simulations. (**D**) Model prediction of the dynein comet size at the MT plus-end breaking homogeneity by setting P_2(tip) different from P_2 on the last 500 nm of the MT. Using the measured value of P_2 and an assumption of homogeneity predicts ∼25 motors in the comet (blue arrow 1). For a lower value $P_2(\text{tip}) \approx 0.55P_2$ the comet size is ∼55 dynein motors (blue arrow 2).

density in the comet serves as a 'buffer stop' for arriving EEs. We carefully analysed the distribution of dynein within comets of various intensities and always found a steady increase of the motor density towards the MT plus-ends (Figure 7A and B). Consistent with the idea that EEs get loaded onto dynein in a stochastic way, they often turned before they have reached the highest dynein density in the comet (Figure 7C, red line represents dynein in the comet, green lines are moving EEs). However, the turning rate increased with an increase in dynein numbers (Figure 7D), suggesting that the probability that EEs get captured by dynein rises within the comet. These results supported the idea that the cell maintains a high number of dynein in order to reduce the risk that EEs detach from or 'fall off' the end of their track. To test this possibility, we reduced the comet size by expressing Peb1c in hyphal cells that also contained GFPRab5a-labelled EEs. Indeed, when only the stochastic dynein population was left, the number of EEs that detached at the end of the MT significantly increased (9.22%; Figure 7E). These results are consistent with a function of the dynein comet being the capture EEs through a stochastic loading process.

Discussion

Bidirectional transport along MTs is an important process that underlies the function and survival of animal cells (Gross, 2004; Welte, 2004; Chevalier-Larsen and Holzbaur, 2006). In this study, we have used a fungal model system to address the question how organelles are kept on track when they reach the end of a MT? It was previously suggested that dynein accumulates at the MT plus-end in an inactive state to receive arriving EEs for retrograde transport (Lenz *et al*, 2006; Abenza *et al*, 2009). We show here that this simple concept needs to be revised. We provide evidence that dynein does not need to be activated but leaves the MT end randomly, suggesting that EEs get loaded onto dynein motors via a stochastic mechanism. In order to increase the probability that arriving organelles meet a dynein motor, the cell accumulates a large number of dynein motors. This is done in two ways (1) an active retention of dynein motors via an interaction between dynein/dynactin and the plus-end binding protein EB1 (=Peb1) and (2) a stochastic process that appears to require no active control but is a consequence of the motility behaviour of motors (Figure 8). This mechanism avoids the cargo from falling off and ensures high fidelity of the transport process.

Dynein is anchored at MT plus-ends by an interaction of dynactin and EB1

In the elongated hyphal cells of fungi, dynein forms comet-like accumulations at the plus-ends of MTs (Han *et al*, 2001; Lenz *et al*, 2006). In this study, we have established nuclear pores as an internal calibration standard and found that an average of 55 motors concentrate in the comet. Dynein is a huge protein complex (King, 2000), making it unlikely that such a large number of motors concentrates at the MT plus-end without serving a cellular function. In mammalian cells, dynactin interacts with the plus-end binding protein EB1 (Ligon *et al*, 2003) and the interaction site is well characterized (Honnappa *et al*, 2006). It was shown that phosphorylation of p150$^{\text{glued}}$ releases the complex from MT plus-ends and allows retrograde organelle motility (Vaughan *et al*, 2002). Our results described here argue that a similar mechanism is

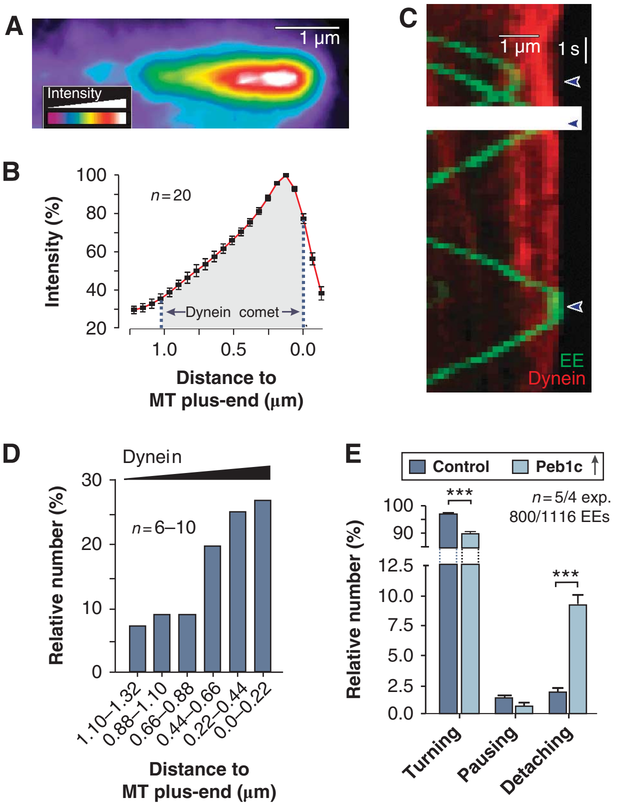

Figure 7 Dynein numbers and EE escape rate at MT plus-ends. (**A**) Pseudo-coloured image of an apical dynein comet (strain AB33G$_3$Dyn2). The bar represents one micrometer. (**B**) Graph showing intensity profile along the length of the dynein comet. Values are mean ± standard error of the mean of linescan analysis of 20 apical dynein comets. Note that the distribution of the dynein along the length of the MT is independent of the overall intensity of the comet. (**C**) Kymograph showing the arrival and turning of photoactivated paRab5a-carrying EEs (green lines) and dynein heavy chain fused to a triple mCherry tag (red). Note that only one of the EEs arrived at the very end of the MT, where dynein concentration is highest. (**D**) Turning of arriving EEs within the dynein comet. Note that the MT plus-end was defined by the maximum intensity of the dynein signal in the comet. (**E**) Bar chart showing the behaviour of EEs in control and cells expressing the peptide Peb1c. Note that Peb1c reduces the average number of dyneins to ~20, which results in 9.22% loss of EEs at the MT end. Triple asterisks indicate significant difference to control at $P<0.0001$.

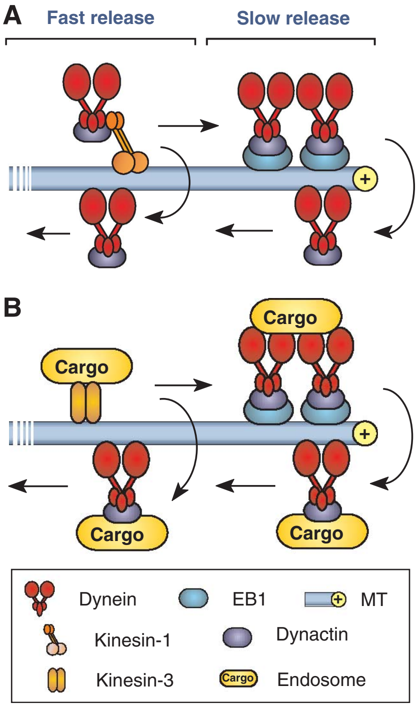

Figure 8 Model of the formation and function of the apical dynein comet. (**A**) Dynein is targeted to plus-ends by kinesin-1. About half of the motors are rapidly turned over (fast release) whereas the other half gets trapped at the MT plus-ends. This involves an interaction between dynactin and the plus-end binding EB1 (=Peb1). This active retention is implicated in the observed slow release of dynein. (**B**) EEs get delivered by kinesin-3. Loading of the cargo onto dynein is a stochastic process that is most likely when the dynein density reaches its maximum.

conserved in fungi, although the dynactin/dynein complex is already assembled at the plus-ends. In addition, we found evidence for a population of more dynamic dynein that is rapidly turned over at the MT plus-end. We assumed that these dynein motors are not anchored at plus-ends, but instead are accumulating as a ‘traffic jam’ of arriving motors. A similar stochastic accumulation was shown for recombinant kinesin motors *in vitro* (Okada and Hirokawa, 1999), which was argued could be due to local ATP depletion (Chowdhury *et al*, 2005).

A mathematical model suggests that a stochastic mechanism accounts for about one-half of the dynein comet

Recent theoretical approaches have strongly suggested that stochastic properties of motor behaviour may be sufficient to explain bidirectional motility in living cells (Klumpp and Lipowsky, 2005; Gazzola *et al*, 2009; Soppina *et al*, 2009; Hendricks *et al*, 2010; Müller *et al*, 2008, 2010). Based on a previous stochastic two-lane model (Ashwin *et al*, 2010), we developed a more realistic 13-lane model to help us understand how dynein accumulates at the MT plus-end simply as a result of the observed stochastic traffic properties on the MT. Most previous mathematical models have exclusively relied on data from *in vitro* experiments and/or used motility parameters from different motors and different organisms. While the lack of consistent data has made this necessary, one should recognize that motors from different organisms or cell types may have very different features. An illustrating example is the difference in the *in vitro* transport velocity of kinesin-1 from animals (~0.4–0.8 μm/s; Vale *et al*, 1985; Porter *et al*, 1987; Bloom *et al*, 1988; Ingold *et al*, 1988) and from fungi (~2–2.5 μm/s; Steinberg and Schliwa, 1996; Steinberg, 1997; Steinberg *et al*, 1998). In our model we also included *in vitro* results from other systems and assume that motors move in multiples of 8 nm steps (Schnitzer and Block, 1997; Reck-Peterson *et al*, 2006) along the 13 protofilaments of the MT (Tilney *et al*, 1973). In contrast to Ashwin *et al* (2010), we consider that dynein is able to change lanes (Wang *et al*, 1995), whereas kinesin-1, which is thought to be the motor for dynein delivery (Zhang *et al*, 2003; Lenz *et al*, 2006), keeps on its protofilament with high fidelity (Ray *et al*, 1993). The remaining parameters in our 13-lane model are based on a quantitative analysis of dynein numbers and motility behaviour in the living cell. Indeed, the 13-lane model nicely predicts that about one-half of the dynein motors in the comet can be found, simply by assuming stochastic transport processes. This number is in good agreement with the amount of dynein that is left at plus-ends when the Dynactin/EB1 interaction is blocked by inhibitory peptides. However, the model assumes homogeneity of motor behaviour along the length of the MT, that is it assumes that turning rates along the track are the same as turning rates at the end of the MT. This is clearly an oversimplification, as the MT plus-end binds numerous proteins (Akhmanova and Steinmetz, 2008) that may occupy sites or influence the tug-of-war between dynein-delivering kinesin-1 and opposing dynein. The assumed presence of additional plus-end binding proteins is also indicated by the fact that the comet stretches over ∼700 nm (see above, Figure 7A), which is larger than the comet length predicted by our model, and which might reflect that motors and plus-end binding proteins compete for binding at MT ends. Such competition could influence the probability for turning from anterograde to retrograde motility, which in our model is described by the probability P_2 per simulation time step. Our data show that varying this P_2 near the tip has a very significant influence on the comet size and can result in much higher numbers of motors at the plus-end. A change in P_2 would also be the consequence of active retention of dynein/dynactin by interaction with EB1. Thus, local conditions at the MT end also influence the comet size in our model. Nevertheless, our model demonstrates that such local conditions are not necessary to predict an accumulation of motors at the plus-end.

The comet serves as a 'buffer stop' for arriving endosomes

Our experiments clearly show that the cell actively concentrates dynein at MT plus-ends to form a comet, which argues for a biological function of the comet. It was previously suggested that the dynein comet serves as a 'dynein loading zone' for arriving endosomes (Lenz *et al*, 2006) that mediate recycling processes to support tip growth of the hyphal cell (Abenza *et al*, 2009; Wedlich-Söldner *et al*, 2000; reviewed in Peñalva, 2010). Indeed, apical recycling makes it necessary that EEs reach the hyphal tip, which increases the risk of EEs falling off the track and requires an efficient capture mechanism. Our results suggest that the dynein comet is part of such a MT-end capture mechanism. We show that dynein is stochastically released from the comet and that EEs have a higher probability to turn around in regions of high dynein numbers. This suggests that the EEs get loaded onto dynein in a stochastic way with the comet serving as a dynamic 'buffer stop'. While our result argue for a function of the comet in capturing arriving organelles, it need to be considered that the apical dynein might also support other functions, such as control of MT length (Adamikova *et al*, 2004) or the retrograde transport of other cargo, such as RNA-binding particles (Becht *et al*, 2006).

Conclusions

Long-range organelle transport is important for numerous aspect of eukaryotic cell function. How motors cooperate in endosome motility is currently under intensive investigation (Soppina *et al*, 2009), but what happens to organelles and motors at the end of the track is not well understood. We show here that the cell uses the stochastic behaviour of the motors on the track and active retention to increase the number of dynein at the tip. Given a stochastic loading process, this ensures that an arriving organelle ultimately finds a dynein to which it can bind for retrograde transport. Recent work has started to highlight the importance of the stochastic behaviour of motor in bidirectional transport processes (Klumpp and Lipowsky, 2005; Müller *et al*, 2008; Gazzola *et al*, 2009) or in controlling MT length (Hough *et al*, 2009). In combination with higher-order regulation, the stochastic transport properties of motors might underlie the complexity of cargo movement in the cell (Müller *et al*, 2008; Welte and Gross, 2008). Our results add to this emerging picture and in particular expand our understanding of motor cooperation in EE motility. However, the biological reason for the bidirectional long-range EE transport is still elusive. Addressing this question is a fascinating challenge for future research.

Materials and methods

Strains and plasmids

The strains $AB33G_3Dyn2$, FB2N107G_ER, FB2N107R-N214G and $FB1Dyn2^{ts}$ were described previously (Wedlich-Söldner *et al*, 2002b; Lenz *et al*, 2006; Theisen *et al*, 2008). To visualize EEs either GFP, paGFP or mCherry were individually fused to the endosome-specific Rab5a (Fuchs *et al*, 2006) under the control of the constitutive *otef* promoter (Spellig *et al*, 1996) and the resulting plasmids were integrated ectopically into the genome of *U. maydis*. Dynein was visualized by labelling the endogenous copy of *dyn*2 with 3GFP, 3paGFP or 3mCherry. The rigor alleles of kinesin-3 as well as the short fragments of the EB1-like plus-end binding protein (Peb1) and the Dynactin subunit p150Glued were expressed as an additional copy under the conditional arabinose-induced *crg* promoter (Bottin *et al*, 1996). Monomeric RFP was fused to the endogenous copy of Peb1 to visualize the plus-ends of MTs. Nuclear pores were visualized by homologous integration of single, double or triple GFP into the native locus of Nup107, Nup214 or Nup2. Various GFP-tagged nucleoporins were combined in single strains to achieve stronger fluorescent signals that could be related to defined numbers of GFP tags. The genotypes of all strains used in this work are summarized in Table I.

Growth conditions

All *U. maydis* cultures were grown overnight at 28°C in complete medium (CM) (Holliday, 1974) containing 1% (w/v) glucose, shaking at 200 revolutions per minute (r.p.m.). Hyphal growth was induced by shifting in NM liquid medium supplemented with 1% (w/v) glucose. Colony growth of strains AB33, a temperature sensitive mutant strain $FB1Dyn2^{ts}$, $AB33G_3Dyn2$ and $AB33pa_mG_{3\text{-}}$Dyn2 was analysed on CM-G plates at 32°C. The expression of genes under the control of the *crg* promoter was introduced by changing the carbon source form glucose to 1% (w/v) arabinose.

Freeze-fracture electron microscopy and Laser-based epifluorescence microscopy

Ultrastructural analysis of nuclear pores were done as described (Severs, 2007; see Supplementary data for details). For light microscopy, cells were placed on a thin layer of 2% agarose, covered with a cover slip, and immediately observed using a IX81 motorized inverted microscope (Olympus, Hamburg, Germany) and a VS-LMS4 Laser-Merge-System solid-state lasers using a 50 or 75 mW observation lasers at 488 and 561 nm. Photoactivation and photobleaching experiments were performed using a Visitron 2D FRAP system. Images were captured using a charged-coupled device camera (Photometric CoolSNAP HQ2, Roper Scientific, Germany). All parts of the system were under the control of the software package MetaMorph (Molecular Devices, Downingtown), which was also used for fluorescence measurements and image processing. For quantitative analysis, images were taken below light saturation and corrected for the adjacent background. See Supplementary data for further details.

Quantitative analysis of fluorescent intensities

For intensity measurements of Nup107-GFP and other GFP-nucleoporins, images were taken at 50 or 250 ms exposure time, focusing on the upper area of the nucleus. Only those signals were analysed for their integrated intensity that (1) were far enough apart from other pores to be measured and (2) were located in the central one square micrometer of the observation field. All measurements were corrected for the background in the nuclear envelope. All corrected values were plotted and the average integrated intensity value for a single Nup107-GFP was calculated. The number of motors was estimated by comparing the corrected integrated intensity values for GFP_6-dynein with the average value of the background-corrected integrated intensity values of a single Nup107-GFP. For each motor measurement, nuclear pore intensities were measured at the same day under the same conditions. To analyse the signal intensity in cells overexpressing the inhibitory peptides Peb1c or Dya1n, the integrated intensity of a single loading zone was recorded. The measured values were background corrected as described above.

Protein extraction and immunodetection

Protein extraction and immunodetection was performed as described (Straube *et al*, 2001). For detection of GFP_3–Dyn2, a monoclonal anti-GFP antibody was used (Roche Diagnostic GmbH, Mannheim, Germany). As secondary antibody, an anti-mouse peroxidase-conjugated antibody was used (Promega, Southampton, UK). Chemiluminescence was detected using the ECL Plus Western Blot detection reagent, following the manufacture's instructions (GE Healthcare, Uppsala, Sweden).

Activation of photoactivatable dynein and photoactivatable Rab5a

For experiments that monitored the decay of pa_mG_3Dyn2, the hyphal tip was irradiated for 25 ms using 2% output power of a solid state 60 mW 405 nm laser, followed by observation using the 488-nm laser at 15% power. A reference image was taken immediately after activation. After 15, 30, 45, 60 s and then every minute a *Z*-stack with 3 plains and a *Z*-distance of 0.25 μm was taken. In a maximum projection, the integrated intensity of the apical accumulation was measured and corrected by the background that was measured in a neighbouring area within the cell. The intensity of the signal at time zero was set to 100% and the intensity of the following time points were correlated to this. Photoactivatable Rab5a was activated like pa_mG_3Dyn2 (see above) and movies with 100 plains at 150 ms exposure time at 20% of the 488-nm laser were taken.

Fluorescent recovery after photobleaching experiments and photobleaching analysis

Dynein motility was analysed after photobleaching using a Visitron 2D FRAP system (Visitron Systems, Munich, Germany) with a solid state 60 mW 405 nm laser. This was followed by observation using the 488-nm observation laser. Velocity, frequency and turning rates/mean run lengths were analysed in kymographs that were generated from these image series using MetaMorph. For stepwise photobleaching experiments, dynein signals (and the internal calibration standard GFP-Nup107) were immobilized using 100 μM CCCP (carbonyl cyanide *m*-chlorophenyl-hydrazone; Sigma-Aldrich Ltd, Gillingham, UK) and bleaching was recorded using the 488-nm observation laser at 5.6 mW laser power were taken. The average intensity of signals was corrected for the background and the number of bleaching steps were determined by a step-find algorithm (Kerssemakers *et al*, 2006) kindly provided by Dr Jacob Kerssemakers, Delft, The Netherlands) in the program MatLab (The MathWorks, Natick). For a more detailed description of both models, see Supplementary data.

Determination of the dynein flux from bleaching-step analysis

Bleaching-step distributions were fit to a sum of normal distributions using the software Prism (GraphPad, San Diego). From this the ratio of 1 dynein:2 dyneins was determined and the measured fluxes of GFP_3–Dyn2 signals were corrected. The mean value of anterograde and retrograde fluxes was used in the mathematical modelling. For a more detailed description of both models, see Supplementary data.

Mathematical modelling

The mathematical model represents an ASEP-type model, extended from a two-lane model for bidirectional motor motion (Ashwin *et al*, 2010). The model makes the following assumptions: (1) motors take multiples of 8 nm steps forward at fixed rate per time step, unless the site to be moved into is already occupied; (2) motion takes place in both directions over 13 lanes corresponding to protofilaments of an MT; (3) motors do not fall off along the track but a minor loss of 2% of the delivered dynein occurs at the tip; (3) dynein changes lanes on average 5.1-times per micrometer (corresponding to experimental data of Wang *et al* (1995)); and (4) kinesin-1 delivering dynein to the plus-end does not change lanes (Ray *et al*, 1993). These assumptions and the experimental measurements were used to determine all rates in the model. Simulations were done using C++ (http://sourceforge.net/projects/dev-cpp/). For a more detailed description of both models, see Supplementary data.

Non-linear regression and statistical analysis

Non-linear regression and all statistical tests were done using the software Prism (GraphPad). Comparison of one-phase decay and two-phase decay models in Figure 4 was done using an F-test ($\alpha = 0.05$). The half-lives of the decay and the proportions in each population are the fitting parameters for a signal that is normalized to lie between 0 and 100%. For further details see Supplementary data.

Supplementary data

Supplementary data are available at *The EMBO Journal* Online (http://www.embojournal.org).

Acknowledgements

This project was supported by the Biotechnology and Biology Research Council (BBSRC; BB/F022956/1), the Deutsche Forschungsgemeinschaft (DFG; STE 799/4-3 and SFB593) and the Max-Planck Institute for Terrestrial Microbiology, Marburg. Dr I Schuchardt and G Fink are gratefully acknowledged for cloning and establishing the photoactivatable GFP-Rab5a construct. Dr Jacob Kerssemakers is gratefully acknowledged for help with the bleaching-step analysis. Finally, we thank the referees of this work for their input, which allowed us to significantly improve the manuscript.

Author contributions: MS has performed most experiments and analysed the data; SK has designed the inhibitory peptides and generated strains; PA and CL have developed the mathematical model and did the statistical analysis; NJS has provided the freeze-fracture EM results; GS has conceived the project, designed and analysed the data, supported the modelling, wrote the manuscript, analysed the experiments and provided overall project management.

Conflict of interest

The authors declare that they have no conflict of interest.

References

Abenza JF, Pantazopoulou A, Rodriguez JM, Galindo A, Penalva MA (2009) Long-distance movement of *Aspergillus nidulans* early endosomes on microtubule tracks. *Traffic* **10:** 57–75

Adamikova L, Straube A, Schulz I, Steinberg G (2004) Calcium signaling is involved in dynein-dependent microtubule organization. *Mol Biol Cell* **15:** 1969–1980

Akhmanova A, Steinmetz MO (2008) Tracking the ends: a dynamic protein network controls the fate of microtubule tips. *Nature Rev* **9:** 309–322

Ally S, Jolly AL, Gelfand VI (2008) Motor-cargo release: CaMKII as a traffic cop. *Nat Cell Biol* **10:** 3–5

Andersson TP, Svensson SP, Karlsson AM (2003) Regulation of melanosome movement by MAP kinase. *Pigment Cell Res* **16:** 215–221

Ashwin P, Lin C, Steinberg G (2010) Queueing induced by bidirectional motor motion near the end of a microtubule. *Phys Rev E* **82:** 051907

Becht P, Konig J, Feldbrugge M (2006) The RNA-binding protein Rrm4 is essential for polarity in *Ustilago maydis* and shuttles along microtubules. *J Cell Sci* **119:** 4964–4973

Bloom GS, Wagner MC, Pfister KK, Brady ST (1988) Native structure and physical properties of bovine brain kinesin and identification of the ATP-binding subunit polypeptide. *Biochemistry* **27:** 3409–3416

Bottin A, Kämper J, Kahmann R (1996) Isolation of a carbon source-regulated gene from *Ustilago maydis*. *Mol Gen Genet* **253:** 342–352

Cai D, Verhey KJ, Meyhöfer E (2007) Tracking single kinesin molecules in the cytoplasm of mammalian cells. *Biophys J* **92:** 4137–4144

Chevalier-Larsen E, Holzbaur EL (2006) Axonal transport and neurodegenerative disease. *Biochim Biophys Acta* **1762:** 1094–1108

Chowdhury D, Schadschneider A, Nishinari K (2005) Physics of transport and traffic phenomena in biology: from molecular motors and cells to organisms. *Phy Life Rev* **2:** 318–352

Deacon SW, Nascimento A, Serpinskaya AS, Gelfand VI (2005) Regulation of bidirectional melanosome transport by organelle bound MAP kinase. *Curr Biol* **15:** 459–463

Fuchs U, Hause G, Schuchardt I, Steinberg G (2006) Endocytosis is essential for pathogenic development in the corn smut fungus *Ustilago maydis*. *Plant Cell* **18:** 2066–2081

Gazzola M, Burckhardt CJ, Bayati B, Engelke M, Greber UF, Koumoutsakos P (2009) A stochastic model for microtubule motors describes the *in vivo* cytoplasmic transport of human adenovirus. *PLoS Comput Biol* **5:** e1000623

Gross SP (2004) Hither and yon: a review of bi-directional microtubule-based transport. *Phys Biol* **1:** R1–R11

Hammond JW, Cai D, Blasius TL, Li Z, Jiang Y, Jih GT, Meyhofer E, Verhey KJ (2009) Mammalian Kinesin-3 motors are dimeric *in vivo* and move by processive motility upon release of autoinhibition. *PLoS Biol* **7:** e72

Han G, Liu B, Zhang J, Zuo W, Morris NR, Xiang X (2001) The *Aspergillus* cytoplasmic dynein heavy chain and NUDF localize to microtubule ends and affect microtubule dynamics. *Curr Biol* **11:** 719–724

Hendricks AG, Perlson E, Ross JL, Schroeder III HW, Tokito M, Holzbaur EL (2010) Motor coordination via a tug-of-war mechanism drives bidirectional vesicle transport. *Curr Biol* **20:** 697–702

Hoepfner S, Severin F, Cabezas A, Habermann B, Runge A, Gillooly D, Stenmark H, Zerial M (2005) Modulation of receptor recycling and degradation by the endosomal kinesin KIF16B. *Cell* **121:** 437–450

Holliday R (1974) *Ustilago maydis*. In *Handbook of Genetics*, King RC (ed) Vol. 1, pp 575–595. New York: Plenum Press

Honnappa S, Okhrimenko O, Jaussi R, Jawhari H, Jelesarov I, Winkler FK, Steinmetz MO (2006) Key interaction modes of dynamic +TIP networks. *Mol Cell* **23:** 663–671

Hough LE, Schwabe A, Glaser MA, McIntosh JR, Betterton MD (2009) Microtubule depolymerization by the Kinesin-8 motor Kip3p: a mathematical model. *Biophys J* **96:** 3050–3064

Howe CL, Mobley WC (2005) Long-distance retrograde neurotrophic signaling. *Curr Opin Neurobiol* **15:** 40–48

Ingold AL, Cohn SA, Scholey JM (1988) Inhibition of kinesin-driven microtubule motility by monoclonal antibodies to kinesin heavy chains. *J Cell Biol* **107:** 2657–2667

Joglekar AP, Salmon ED, Bloom KS (2008) Counting kinetochore protein numbers in budding yeast using genetically encoded fluorescent proteins. *Methods Cell Biol* **85:** 127–151

Kerssemakers JW, Munteanu EL, Laan L, Noetzel TL, Janson ME, Dogterom M (2006) Assembly dynamics of microtubules at molecular resolution. *Nature* **442:** 709–712

King SM (2000) The dynein microtubule motor. *Biochim Biophys Acta* **1496:** 60–75

Klumpp S, Lipowsky R (2005) Cooperative cargo transport by several molecular motors. *Proc Natl Acad Sci USA* **102:** 17284–17289

Kumar S, Lee IH, Plamann M (2000) Cytoplasmic dynein ATPase activity is regulated by dynactin-dependent phosphorylation. *J Biol Chem* **275:** 31798–31804

Lenz JH, Schuchardt I, Straube A, Steinberg G (2006) A dynein loading zone for retrograde endosome motility at microtubule plus-ends. *EMBO J* **25:** 2275–2286

Ligon LA, Shelly SS, Tokito M, Holzbaur EL (2003) The microtubule plus-end proteins EB1 and dynactin have differential effects on microtubule polymerization. *Mol Biol Cell* **14:** 1405–1417

Lomakin AJ, Semenova I, Zaliapin I, Kraikivski P, Nadezhdina E, Slepchenko BM, Akhmanova A, Rodionov V (2009) CLIP-170-dependent capture of membrane organelles by microtubules initiates minus-end directed transport. *Dev Cell* **17:** 323–333

Miaczynska M, Pelkmans L, Zerial M (2004) Not just a sink: endosomes in control of signal transduction. *Curr Opin Cell Biol* **16:** 400–406

Müller MJ, Klumpp S, Lipowsky R (2008) Tug-of-war as a cooperative mechanism for bidirectional cargo transport by molecular motors. *Proc Natl Acad Sci USA* **105:** 4609–4614

Müller MJ, Klumpp S, Lipowsky R (2010) Bidirectional transport by molecular motors: enhanced processivity and response to external forces. *Biophysical J* **98:** 2610–2618

Münsterkötter M, Steinberg G (2007) The fungus *Ustilago maydis* and humans share disease-related proteins that are not found in *Saccharomyces cerevisiae*. *BMC Genomics* **8:** 473

Okada Y, Hirokawa N (1999) A processive single-headed motor: kinesin superfamily protein KIF1A. *Science* **283:** 1152–1157

Patterson GH, Lippincott-Schwartz J (2002) A photoactivatable GFP for selective photolabeling of proteins and cells. *Science* **297:** 1873–1877

Peñalva MA (2010) Endocytosis in filamentous fungi: Cinderella gets her reward. *Curr Opin Microbiol* **13:** 1–9

Porter ME, Scholey JM, Stemple DL, Vigers GP, Vale RD, Sheetz MP, McIntosh JR (1987) Characterization of the microtubule movement produced by sea urchin egg kinesin. *J Biol Chem* **262:** 2794–2802

Rabut G, Doye V, Ellenberg J (2004) Mapping the dynamic organization of the nuclear pore complex inside single living cells. *Nat Cell Biol* **6:** 1114–1121

Ray S, Meyhöfer E, Milligan RA, Howard J (1993) Kinesin follows the microtubule's protofilament axis. *J Cell Biol* **121:** 1083–1093

Reck-Peterson SL, Yildiz A, Carter AP, Gennerich A, Zhang N, Vale RD (2006) Single-molecule analysis of dynein processivity and stepping behavior. *Cell* **126:** 335–348

Schnitzer MJ, Block SM (1997) Kinesin hydrolyses one ATP per 8-nm step. *Nature* **388:** 386–390

Schroer TA (2004) Dynactin. *Annu Rev Cell Dev Biol* **20:** 759–779

Schuchardt I, Assmann D, Thines E, Schuberth C, Steinberg G (2005) Myosin-V, Kinesin-1, and Kinesin-3 cooperate in hyphal growth of the fungus *Ustilago maydis*. *Mol Biol Cell* **16:** 5191–5201

Severs NJ (2007) Freeze-fracture electron microscopy. *Nat Protoc* **2:** 547–576

Soppina V, Rai AK, Ramaiya AJ, Barak P, Mallik R (2009) Tug-of-war between dissimilar teams of microtubule motors regulates transport and fission of endosomes. *Proc Natl Acad Sci USA* **106:** 19381–19386

Spellig T, Bottin A, Kahmann R (1996) Green fluorescent protein (GFP) as a new vital marker in the phytopathogenic fungus *Ustilago maydis*. *Mol Gen Genet* **252:** 503–509

Steinberg G (1997) A kinesin-like mechanoenzyme from the zygomycete *Syncephalastrum racemosum* shares biochemical similarities with conventional kinesin from *Neurospora crassa*. *Eur J Cell Biol* **73:** 124–131

Steinberg G (2007) On the move: endosomes in fungal growth and pathogenicity. *Nat Rev Microbiol* **5:** 309–316

Steinberg G, Perez-Martin J (2008) *Ustilago maydis*, a new fungal model system for cell biology. *Trends Cell Biol* **18:** 61–67

Steinberg G, Schliwa M (1996) Characterization of the biophysical and motility properties of kinesin from the fungus *Neurospora crassa*. *J Biol Chem* **271:** 7516–7521

Steinberg G, Schliwa M, Lehmler C, Bölker M, Kahmann R, McIntosh JR (1998) Kinesin from the plant pathogenic fungus *Ustilago maydis* is involved in vacuole formation and cytoplasmic migration. *J Cell Sci* **111:** 2235–2246

Straube A, Brill M, Oakley BR, Horio T, Steinberg G (2003) Microtubule organization requires cell cycle-dependent nucleation at dispersed cytoplasmic sites: polar and perinuclear microtubule organizing centers in the plant pathogen *Ustilago maydis*. *Mol Biol Cell* **14:** 642–657

Straube A, Enard W, Berner A, Wedlich-Söldner R, Kahmann R, Steinberg G (2001) A split motor domain in a cytoplasmic dynein. *EMBO J* **20:** 5091–5100

Theisen U, Straube A, Steinberg G (2008) Dynamic rearrangement of nucleoporins during fungal 'open' Mitosis. *Mol Biol Cell* **19:** 1230–1240

Tilney LG, Bryan J, Bush DJ, Fujiwara K, Mooseker MS, Murphy DB, Snyder DH (1973) Microtubules: evidence for 13 protofilaments. *J Cell Biol* **59:** 267–275

Ulbrich MH, Isacoff EY (2007) Subunit counting in membrane-bound proteins. *Nat Methods* **4:** 319–321

Vale RD, Reese TS, Sheetz M (1985) Identification of a novel force-generating protein, kinesin, involved in microtubule-based motility. *Cell* **42:** 39–50

Valetti C, Wetzel DM, Schrader M, Hasbani MJ, Gill SR, Kreis TE, Schroer TA (1999) Role of dynactin in endocytic traffic: effects of dynamitin overexpression and colocalization with CLIP-170. *Mol Biol Cell* **10:** 4107–4120

Vallee RB, Williams JC, Varma D, Barnhart LE (2004) Dynein: an ancient motor protein involved in multiple modes of transport. *J Neurobiol* **58:** 189–200

Vaughan KT (2005) Microtubule plus ends, motors, and traffic of Golgi membranes. *Biochim Biophys Acta* **1744:** 316–324

Vaughan PS, Miura P, Henderson M, Byrne B, Vaughan KT (2002) A role for regulated binding of p150(Glued) to microtubule plus ends in organelle transport. *J Cell Biol* **158:** 305–319

Wang Z, Khan S, Sheetz MP (1995) Single cytoplasmic dynein molecule movements: characterization and comparison with kinesin. *Biophys J* **69:** 2011–2023

Wedlich-Söldner R, Bölker M, Kahmann R, Steinberg G (2000) A putative endosomal t-SNARE links exo- and endocytosis in the phytopathogenic fungus *Ustilago maydis*. *EMBO J* **19:** 1974–1986

Wedlich-Söldner R, Schulz I, Straube A, Steinberg G (2002b) Dynein supports motility of endoplasmic reticulum in the fungus *Ustilago maydis*. *Mol Biol Cell* **13:** 965–977

Wedlich-Söldner R, Straube A, Friedrich MW, Steinberg G (2002a) A balance of KIF1A-like kinesin and dynein organizes early endosomes in the fungus *Ustilago maydis*. *EMBO J* **21:** 2946–2957

Welte MA (2004) Bidirectional transport along microtubules. *Curr Biol* **14:** R525–R537

Welte MA, Gross SP (2008) Molecular motors: a traffic cop within? *HFSP J* **2:** 178–182

Xiang X (2003) LIS1 at the microtubule plus end and its role in dynein-mediated nuclear migration. *J Cell Biol* **160:** 289–290

Zhang J, Li S, Fischer R, Xiang X (2003) Accumulation of cytoplasmic dynein and dynactin at microtubule plus ends in *Aspergillus nidulans* is kinesin dependent. *Mol Biol Cell* **14:** 1479–1488

Zhang J, Zhuang L, Lee Y, Abenza JF, Peñalva MA, Xiang X (2010) The microtubule plus-end localization of Aspergillus dynein is important for dynein-early-endosome interaction but not for dynein ATPase activation. *J Cell Sci* **123:** 3596–3604